Complicated lithospheric structure beneath the contiguous US revealed by teleseismic S reflections

Tianze Liu[1], **Peter M. Shearer**[1]

[1]Institute of Geophysics and Planetary Physics, Scripps Institution of Oceanography, UC San Diego

Key Points:

- The LAB in the Western US is 60–110km deep and correlates well with active tectonic processes.
- Two MLDs exist in the Central and Eastern US in the depth range 60–100km and 100–150km, which correlate with past tectonic processes.
- Our results agree well with the results of P receiver functions in many areas.

Corresponding author: Tianze Liu, tianzeliu@ucsd.edu

Abstract

Lithospheric discontinuities, including the lithosphere-asthenosphere boundary (LAB) and the enigmatic mid-lithospheric discontinuities (MLDs), hold important clues about the structure and evolution of tectonic plates. However, P- and S-receiver-function techniques (PRF and SRF), two traditional techniques to image Earth's deep discontinuities, have some shortcomings in imaging lithosphere discontinuities. Here, we propose a new method using reflections generated by teleseismic S waves (hereafter S reflections) to image lithospheric discontinuities, which is less affected by multiple phases than PRFs and has better depth resolution than SRFs. We apply this method to data collected by the Transportable Array and other regional seismic networks and obtain new high-resolution images of the lithosphere below the contiguous US. Beneath the tectonically active Western US, we observe a negative polarity reflector (NPR) in the depth range of 60–110 km, with greatly varying amplitude and depth, which correlates with active tectonic processes. We interpret this feature as the lithosphere-asthenosphere boundary below the Western US. Beneath the tectonically stable Central and Eastern US, we observe two NPRs in the depth ranges of 60–100 km and 100–150 km, whose amplitude and depth also vary significantly, and which appear to correlate with past tectonic processes. We interpret these features as mid-lithospheric discontinuities below the Central and Eastern US. Our results show reasonable agreement with results from PRFs, which have similar depth resolution, suggesting the possibility of joint inversion of S reflections and PRFs to constrain the properties of lithospheric discontinuities.

1 Introduction

The structure of the lithosphere-asthenosphere system is fundamental to understanding plate tectonics and Earth's evolution. Continental lithosphere, which is far more complicated than its oceanic counterpart due to the imprints left by numerous geologic processes during its long life, has drawn great attention from the seismological community (e.g. Rychert et al. (2005), Rychert and Shearer (2009), Levander and Miller (2012), Hansen et al. (2015), Hopper and Fischer (2018), L. Liu and Gao (2018), and Kind et al. (2020)). However, despite decades of efforts in seismically imaging the continental lithosphere, several fundamental questions regarding seismic discontinuities in the lithosphere-asthenosphere system remain open: What is the depth to the lithosphere-asthenosphere boundary (LAB)? Is the LAB a sharp boundary or a transition zone that spans many tens of kilometers? Does the lithosphere have internal layering, which has been invoked to explain the observations of mid-lithospheric discontinuities (MLDs; e.g. Savage and Silver (2008), Ford et al. (2010)), and how do the aforementioned characteristics of lithospheric discontinuities vary across different geologic provinces? These questions motivate further seismic studies to better resolve lithospheric discontinuities beneath continents.

Traditionally, P and S receiver-functions (SRF and PRF) are widely used for imaging lithospheric discontinuities (e.g. Rychert and Shearer (2009), Levander and Miller (2012), Hansen et al. (2015), and Hopper and Fischer (2018)). However, both PRF and SRF have some limitations that hamper their utility in imaging lithospheric interfaces. For PRF, multiple reflected phases generated at the Moho and intra-crustal interfaces arrive in the same time window as P-to-S conversions from lithospheric discontinuities and cause strong interference (Fig. 1d). For SRF, although the S-to-P conversions arrive before direct S and thus do not suffer interference of crustal multiple phases, the significantly lower frequency band of teleseismic S waves than P waves causes SRFs to have lower depth resolution than PRFs (Fig. 1e), which prevents imaging detailed structures within the lithosphere. In addition, the very long periods and small temporal separations between conversions at the Moho and shallow lithospheric discontinuities cause potential interference between the side lobes of the Moho conversions and the lithospheric discontinuity conversions of interest (Kind et al., 2020), further complicating the interpretation of SRF images.

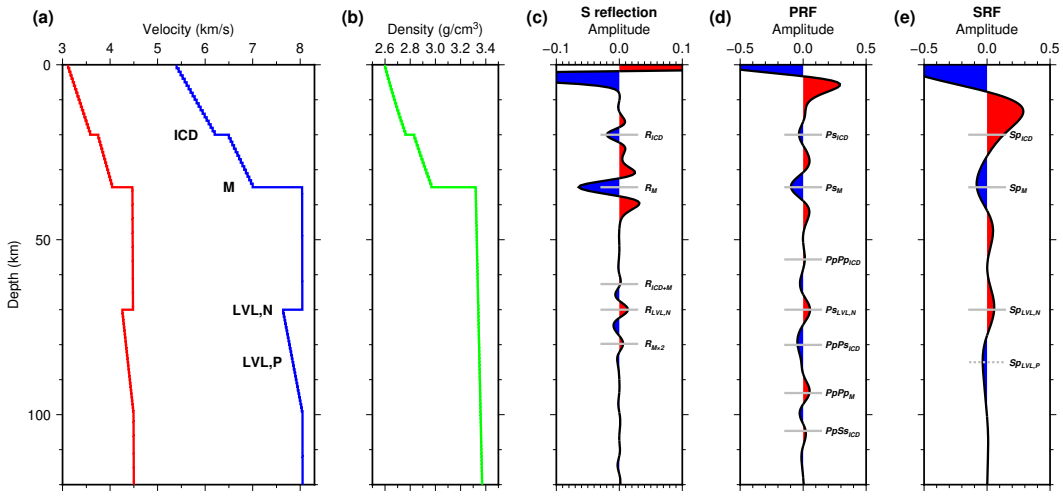

Figure 1. Synthetic examples of imaging lithospheric discontinuities with S reflections, P receiver functions (PRF), and S receiver functions (SRF). The S-reflection and SRF waveforms are computed using a Ricker source wavelet with a median frequency of 0.2 Hz, and the PRF waveform is computed using a Ricker source wavelet with a median frequency of 0.5 Hz (a) 1D V_p (blue) and V_s (red) models used for computing synthetic waveforms. ICD: intra-crustal discontinuity. M: Moho. LVL,N: Negative velocity gradient zone associated with the low-velocity layer (LVL). LVL,P: Positive velocity gradient zone associated with the LVL. (b) 1D density model used for computing synthetic waveforms. (c) S-reflection waveforms computed with the models in (a) and (b) and mapped to depth domain using the same velocity model. (d) P receiver-function waveforms (without deconvolution) computed with the models in (a) and (b) and mapped to depth domain using the same velocity model. (c) S receiver-function waveforms (without deconvolution) computed with the models in (a) and (b) and mapped to depth domain using the same velocity model. Note that the image from teleseismic S reflections has less interference from crustal multiples than the one from PRFs and has higher depth resolution than the one from SRFs.

Recently, Shearer and Buehler (2019) proposed using topside reverberations generated by transverse-component teleseismic S waves to image upper-mantle discontinuities (Fig. 2). This method has two major advantages over PRF and SRF in imaging lithospheric discontinuities. First, multiple reflection phases are much weaker than single reflections because the former undergo additional reflections (Fig. 1c), in contrast to multiples in PRF, which typically have comparable amplitude to the conversions (Fig. 1d). Thus, images of lithospheric discontinuities derived with S reflections suffer less interference from crustal multiples than the ones derived with PRFs (Figs. 1c, d). Second, although both S reflections and SRF utilize long-period teleseismic S waves, the temporal separation between different arrivals is much larger on S reflections than on SRFs because the relative arrival time of the S reflection is the two-way S travel time between the interface and the free surface, whereas the relative arrival time of a conversion on SRF is the difference between the one-way S and P travel times from the interface to the free surface. Thus, for a given interface, the S reflection is separated in time from direct S by a factor of about five compared to the equivalent SRF converted phase, which means that S-reflection imaging provides much better depth resolution than SRF imaging for data over a similar frequency band (Figs. 1c, e). However, a shortcoming of S-reflection imaging is that, for a global discontinuity, an event above it generates reverberations at both the source side and receiver side (Fig. 2), which arrive at approximately the same time and complicate the interpretation of the image. To address this issue, Shearer and Buehler (2019), which used only events shallower than 50km, applied an inversion technique to separate global source-side structure from receiver-side structure beneath the Transportable Array (TA). Despite the success of this approach for imaging the 410- and 660-km discontinuities, it cannot completely eliminate some inherent non-uniqueness between source- and receiver-side structure in the inversion, which could cause artifacts in the resulting images.

To reduce contamination from source-side structure, here we analyze S reflections of earthquakes deeper than 150 km to image receiver-side structures shallower than the event focal depths. In this case, direct topside reflections from a layer above 150 km occur only at the receiver side (Fig. 2), which eliminates the need for the inversion procedure in Shearer and Buehler (2019). Note that underside reflections from interfaces shallower than the event focal depths may be generated near the source, but these arrivals will not stack coherently over varying source depths. We apply this method to data collected by both TA and other regional seismic networks in the contiguous US and create high-resolution images of lithospheric discontinuities below the Moho in the study region. We find that our images agree reasonably well with PRF results in regions with good data coverage and that many prominent features in our images can be related to the the tectonic evolution of the North America continent.

2 Data and methods

We obtained three-component waveform data for events with magnitude > 5.5, focal depth > 150km, and epicentral distance between 30° and 120° recorded at TA and all major regional seismic networks in the contiguous US (see Fig. 3 for a station map and the Acknowledgement for a list of the seismic networks included). Because the vast majority of deep-focus events are hosted in subduction zones, the back azimuths of our records are limited to a few narrow corridors that contain major subduction zones (Fig. 3a). We use a 150-km minimum event depth for two reasons. First, this guarantees that topside reflections for discontinuities between the surface and 150 km are only generated near the receiver, the depth range that we focus on in this study. Second, this assures that depth phases (sS), which are much stronger than internal discontinuity reflections, arrive outside the time window for reflections from interfaces shallower than 150km (Fig. 4a). We then lowpass-filter the traces to below 0.1Hz, downsample them to 1Hz, rotate the horizontal components to radial and transverse components, and align and normal-

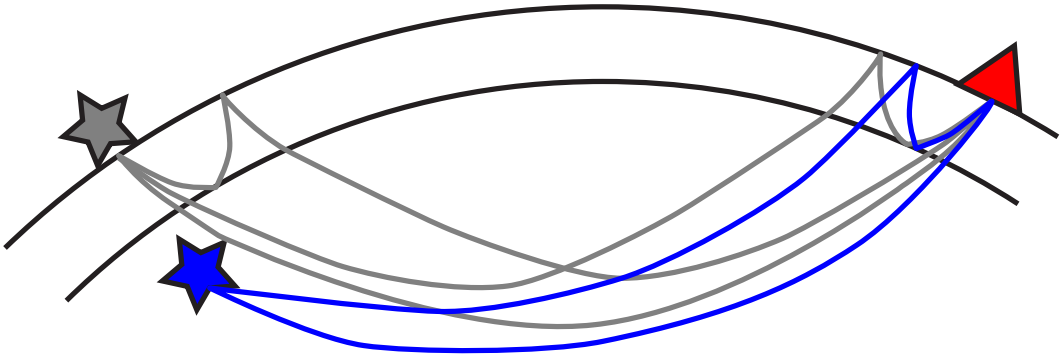

Figure 2. Ray paths of teleseismic S reflections. Note that an event shallower than the discontinuity (gray star) generates both source-side and the receiver-side topside reflections, whereas an event deeper than the discontinuity (blue star) generates only a receiver-side reflection.

ize the transverse components to the maximum amplitude of direct S (Shearer, 1991). We note that although teleseismic S waves should contain some energy up to ~ 0.5Hz, a corner frequency commonly used by SRF studies (e.g. L. Liu and Gao (2018)), we choose a corner frequency of ~ 0.1Hz to improve the coherence of our images and concentrate on resolving only large-scale structure. Future S-reflection studies could use higher-frequency data to study regional fine-scale structure of the lithosphere, especially when data from dense local temporary networks is used. Although our stacked S-wave pulse widths are about two times broader than those seen in typical SRF studies, we nonetheless obtain better depth resolution because the temporal separation between topside S reflections is about five times greater than the separation of equivalent conversions in SRFs.

To assure data quality, we define a $\pm$25s window around the direct S arrival as the source window and retain only the traces that satisfy the following three criteria: First, the ratio between the mean absolute amplitude (MAA) in the source window and the noise window, defined as the 25s before the source window, is > 5, which excludes traces with high noise levels. Second, the ratio between the MAA of the source window and the coda window, defined as the 25s after the source window, is > 1, which excludes traces with abnormally strong coda. Third, the ratio between the maximum amplitude and the MAA in the source window is > 3, which retains only the traces with impulsive source-time functions and thus increases the depth resolution of our images. To further verify our data quality, we plot a record section with the 50,904 traces that passed our selection criteria (Fig. 4a). The record section shows clear direct S and *ScS*, which closely resemble these two phases in Figure 1 in Shearer and Buehler (2019).

We note that our stacking method, both for the record sections discussed here and later when we group data in bins of predicted reflection points, does not involve deconvolution. Rather, we align the traces on the maximum absolute value of the direct S reference phase, flipping the polarity as needed, and normalize the reference peak to unit amplitude. Because these are velocity records, there will typically be a large negative sidelobe either before or after the peak on each trace, so the resulting data stack will have a central peak, with negative sidelobes on each side. Although in principle, these sidelobes might be reduced by using deconvolution or by first correcting the records to displacement, we have found that in practice these approaches can introduce instabilities that complicate interpretation of the results. In contrast, the simple alignment stacking method, when applied to a large number of traces, usually produces a fairly repeatable effective source-time function, which facilitates interpretation and modeling.

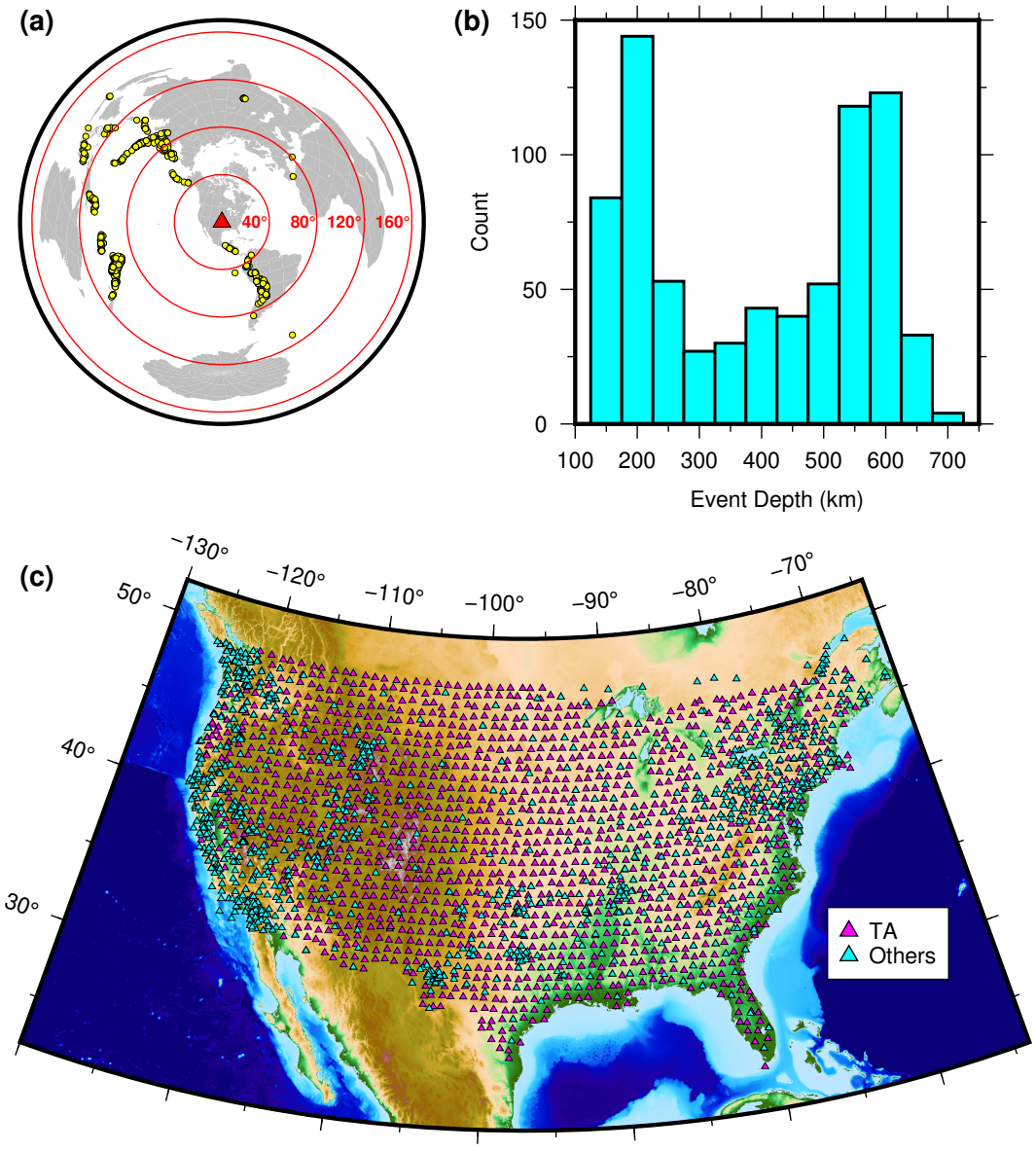

Figure 3. Station and event distribution. (a) Deep events ($\geq$ 150 km) used in our analysis. Concentric circles have radii of 40°, 80°, 120°, and 160°. (b) Depth distribution of the deep events used in our analysis. (c) Stations used in our analysis. Magenta and cyan triangles: The Transportable Array (TA) stations and other regional seismic networks, respectively.

Because we use events deeper than 150km, the part of Figure 4 below the predicted arrival time of *sS* for 150-km focal depth (shown as the gray curve) is dominated by *sS* arrivals and thus does not show clear *Ss410s* and *Ss660s* phases as in Figure 1 of Shearer and Buehler (2019) (which lacked depth-phase interference at those depths owing to the use of shallow events only). The gray curve also marks the arrival time of receiver-side topside S reflections at 150km because the S reflection at a particular depth arrives at approximately the same time as *sS* from an event at that depth. To further reduce the interference of *ScS* and *sS*, we compute their travel times using the IASP91 model (Kennett & Engdahl, 1991) and mute their amplitude using a Hanning taper around their predicted arrival times. The resulting record section shows clearer *Ss410s* and *Ss660s* phases, especially beyond 95°, indicating successful removal of *sS* interference. On the record sections with *ScS* and *sS* muted, we observe a broad band of positive amplitudes in the time window corresponding to reflections between 50 and 150km depth, implying the presence of negative-polarity reflectors (NPRs) in this depth range.

Next, we construct common-reflection-point (CRP) images by tracing all the topside S-reflected rays using the IASP91 model (Kennett & Engdahl, 1991) and stacking the amplitudes corresponding to reflection points at each depth into 2°×2° square cells with 1° overlaps in both W-E and S-N directions. The number of rays stacked for each bin (the fold) varies widely (Fig. 5g), mostly due to the uneven distribution of seismic stations (Fig. 3c), with high stacking fold n along the west coast and the Intermountain West Seismic Zone ($n > 600$; Fig. 5g) and low n in most of the Midwest ($n < 100$; Fig. 5g). The profiles generally show negative arrivals at less than 50 km depth, mostly due to the Moho, and positive arrivals between 50 and 150 km depth, likely due to negative-polarity reflectors (NPRs) in the mantle. In the rest of this paper, a "positive arrival" means an arrival with positive amplitude on our images, which could represent a reflection/conversion at an interface with negative impedance/velocity contrast (NPR in the case of S-reflection images) but could also be an imaging artifact due to sidelobes or multiple reflections. Before discussing the features seen on our S-reflection profiles in detail, we will first present some comparisons to receiver function results.

3 Results

3.1 General comparison between S-reflection, SRF, and PRF profiles

Most previous studies of lithospheric discontinuities beneath the contiguous US were derived with SRF (e.g. Hopper and Fischer (2018) and L. Liu and Gao (2018)). Here we will compare our S-reflection images with the SRF results of Hopper and Fischer (2018), which has similar coverage across the US. To compare our images with PRF, we acquired PRFs of the same seismic networks as our study from the IRIS DMC EarthScope Automated Receiver Survey (EARS) (Crotwell & Owens, 2005). We trace the PRF rays with the IASP91 model (Kennett & Engdahl, 1991) and stack the amplitudes at the conversion points into the same grid cells used for our S-reflection CRP image, which gives a PRF common-conversion-point (CCP) image. We reverse the polarities of the PRFs so that the polarity of an interface is consistent between the CRP and CCP images (positive and negative amplitudes indicate impedance/velocity decreasing and increasing with depth, respectively; Figs. 5, 11, and 12). We extract four W-E profiles A1–A4 and two S-N profiles B1 and B2 (see Fig. 5g for the locations of the profiles) from our S-reflection and PRF image volumes, as well as the SRF image volume of Hopper and Fischer (2018). Fig. 6 shows the comparison between our S-reflection image, the SRF image from Hopper and Fischer (2018), and our PRF image for our W-E Profile A2. Figures S1 and S2 show additional profile comparisons between our results and SRF images from Hopper and Fischer (2018). We flip the polarity of the SRF images so they have the same color convention as the other two images (blue and red indicate impedance/velocity increases and decreases with depth, respectively) and average the SRF model with the same 2°grid cells used in our image.

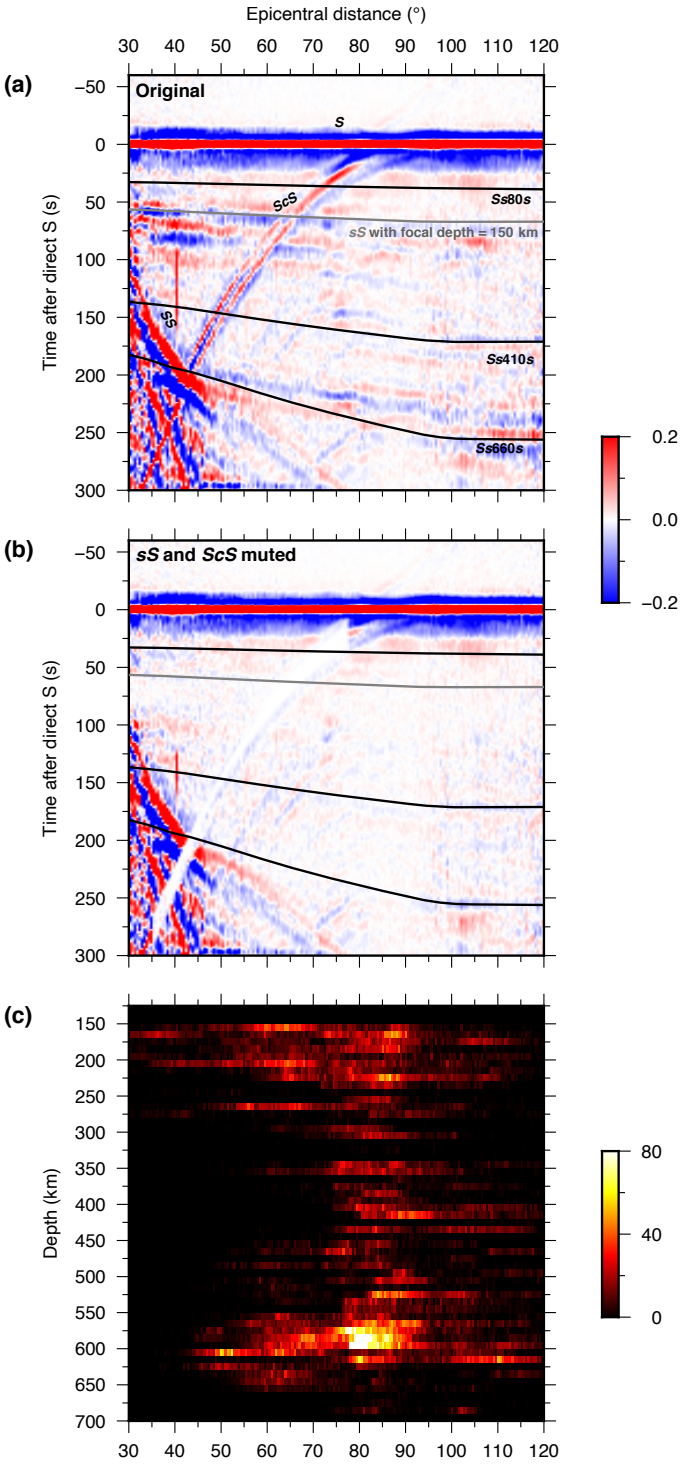

Figure 4. (a) Record section of traces included in our analysis. Note the strong depth phases that overprint reflections deeper than 150 km. The black and gray curves mark the predicted arrival times for reflections at 80, 410, 660km depth, and *sS* for a focal depth of 150 km, respectively. Also note the interference of *ScS*. (b) The same as (a) but with *sS* and *ScS* muted using their predicted arrival times. Note that the 410 and 660 reflections start to emerge after the interfering *sS* phases are muted. (b) Distribution of event depth and distance.

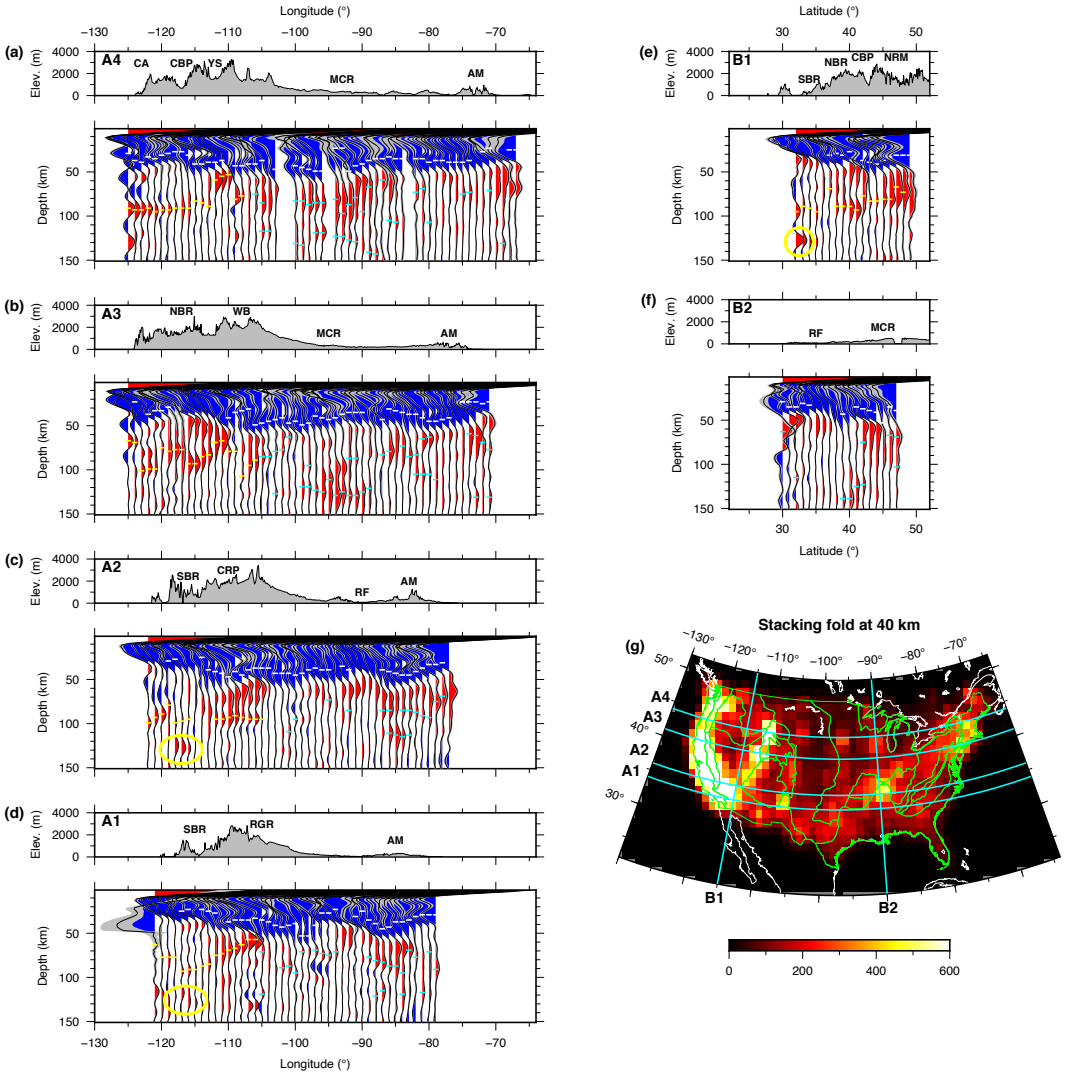

Figure 5. Results derived from our common-reflection-point (CRP) image. (a–d) Reflectivity and topography profiles along 34°N (A1), 36°N (A2), 41°N (A3), and 44°N (A4). Blue and red indicate impedance increasing and decreasing with depth, respectively. The uncertainty of each trace is marked in gray. Yellow, and cyan bars: Our LAB picks in the Western US (WUS) and MLD picks in the Central and Eastern US (CEUS), respectively. Yellow ovals mark NPRs below the LAB in the southern Basin and Range Province. Acronyms of important tectonic features: CA: Cascade Arc; CBP: Columbia Plateau; YS: Yellowstone Hotspot; MCR: Midcontinent Rift; AM: Appalachian Mountains; NBR: northern Basin and Range Province; WB: Wyoming Basin; SBR: southern Basin and Range Province; CRP: Colorado Plateau; RF: Reelfoot Rift; RGR: Rio-Grande Rift; NRM: northern Rocky Mountainl (e) and (f): The same as (a–d), but along 115°W (B1) and 90°W (B2). (g): Stacking fold of our CRP image at 40km depth. Major physiographic provinces of the US (Fenneman, 1946) are plotted in green in (g)

The three images agree reasonably well for depth variations of the Moho, which appears as a negative arrival (impedance/velocity increase with depth) in the depth range 20–50km (Fig. 6). Below the Moho, the profiles often do not agree very well in their details, but their average properties with depth appear similar. Each method shows significant positive arrivals between the Moho and about 100 km depth, although the SRF image is more diffuse, possibly because of its more limited depth resolution. These positive arrivals indicate an impedance/velocity decrease with depth, which SRF studies have interpreted as the LAB in the Western and Eastern US and as an MLD in the Central US (e.g., Hopper and Fischer (2018)).

We note that the positive arrivals immediately below the Moho in our S reflection image are at least partly caused by the sidelobe of the Moho arrivals; however, as we will discuss later they often are stronger than one would expect from the Moho sidelobe alone. The SRFs have undergone deconvolution, but there has been some controversy regarding whether this process could nonetheless produce Moho-related sidelobe artifacts (e.g., Kind et al. (2020). We will discuss this issue more later, but note that the positive arrivals (negative polarity reflectors) that we observe at about 70- to 100-km depth have no Moho sidelobe component and are also widely seen in the SRF images. Details of the arrivals between the Moho and 100 km appear more focused in depth in both our results and the PRF profiles, presumably due to their higher depth resolution, and are sometimes split into more than one apparent interfaces.Between 100 and 150 km, our S reflection image has positive average arrivals, but these arrivals are generally weaker and less continuous than those seen at shallower depths. In contrast, the SRF image has a slightly negative average amplitude over this depth range, although there are occasionally positive amplitude features. The PRF image over this depth range shows some strong features, especially in the west, but is likely contaminated by Moho multiples and thus is difficult to interpret.

Despite differences in resolution, our S-reflection image shows features similar to the other methods in some areas. For example, the positive arrival at $\sim$ 130km depth at $\sim 85°$N appears consistent between our S-reflection image and the SRF image (Fig. 6a, b), and the multiple positive arrivals between 50 and 100km beneath the Colorado Plateau appear very consistent between our S-reflection image and PRF image (Fig. 6a, c). We will now present more detailed descriptions of particular features in our results.

3.2 Moho

We automatically pick the Moho from our data stack at each grid point as the local minima with the largest absolute amplitude in the depth range of 20–60km. In cases where the Moho is not the strongest negative peak in the depth range due to complicated crust and upper-mantle structure, we manually correct the Moho-depth picks to a more appropriate peak based on the Moho picks at adjacent grid points. The resulting Moho-depth map shows good correlation with physiographic provinces (Fig. 7a). The Moho is shallow ($<$ 25km) in the Basin and Range Province, the Columbia Plateau, the Gulf Coast, and the Atlantic Coast, whereas the Moho is deep in the Colorado Plateau, the southern Rocky Mountains, most of the Great Plains, and the Appalachian Mountains. We note that in areas where the Moho is extremely shallow, e.g. the southern Basin and Range, the Moho reflection arrives so early that it merges with the trailing side lobe of the reference pulse (direct S on the stacked trace), causing null Moho detections.

The Moho amplitude also correlates well with the physiographic provinces, with high amplitudes in the Basin and Range Province, the Columbia Plateau, the northern Rocky Mountains, the Gulf Coast, and the Atlantic Coast, and low amplitudes in the Colorado Plateau, the middle Rocky Mountains, the Wyoming Basin, most of the Great Plains, and the Appalachian Mountains (Fig. 7b). Figure 7 compares these results with two previous Moho depth maps obtained using different methods: (1) the *Pn* analysis

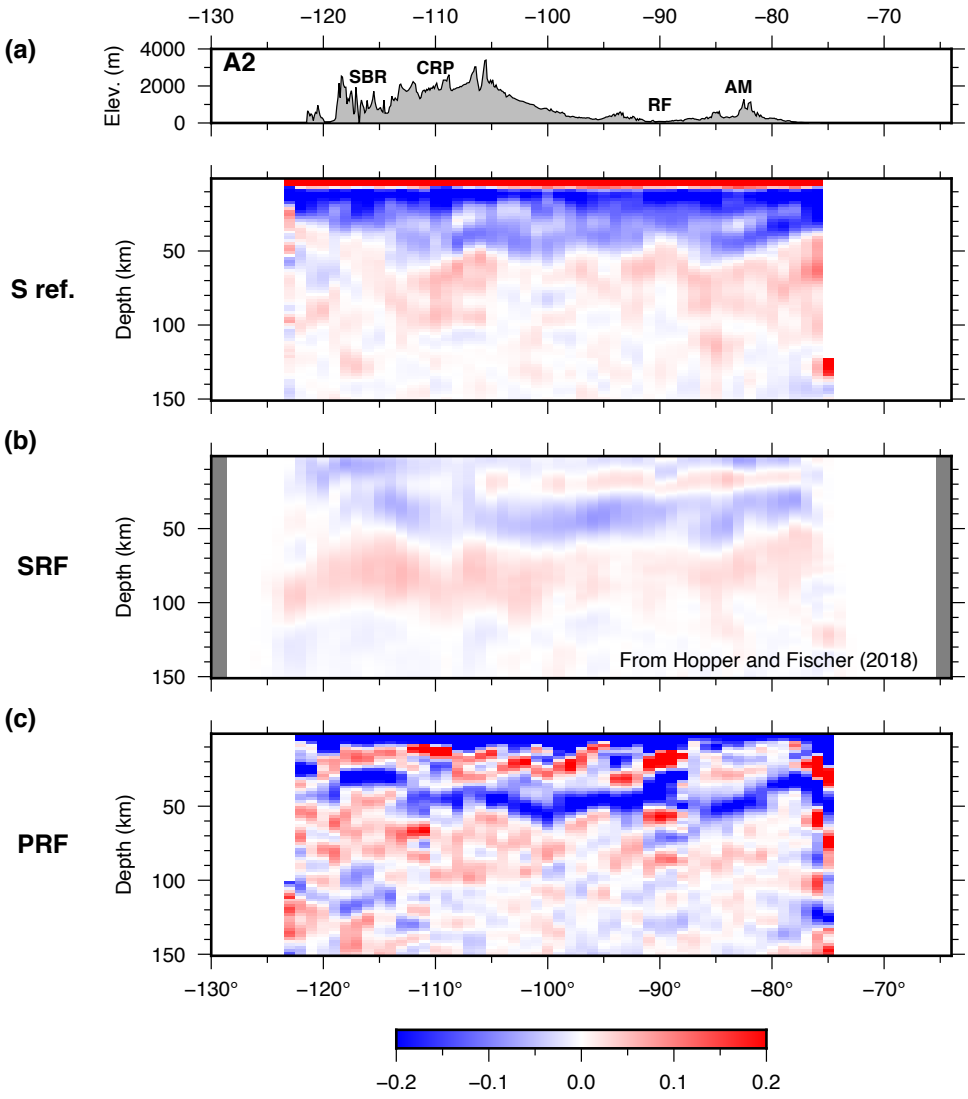

Figure 6. Comparison between (a) our S-reflection image, (b) SRF image from Hopper and Fischer (2018), and (c) our PRF image for Profile A2. Acronyms for key tectonic features are the same as in Fig. 5

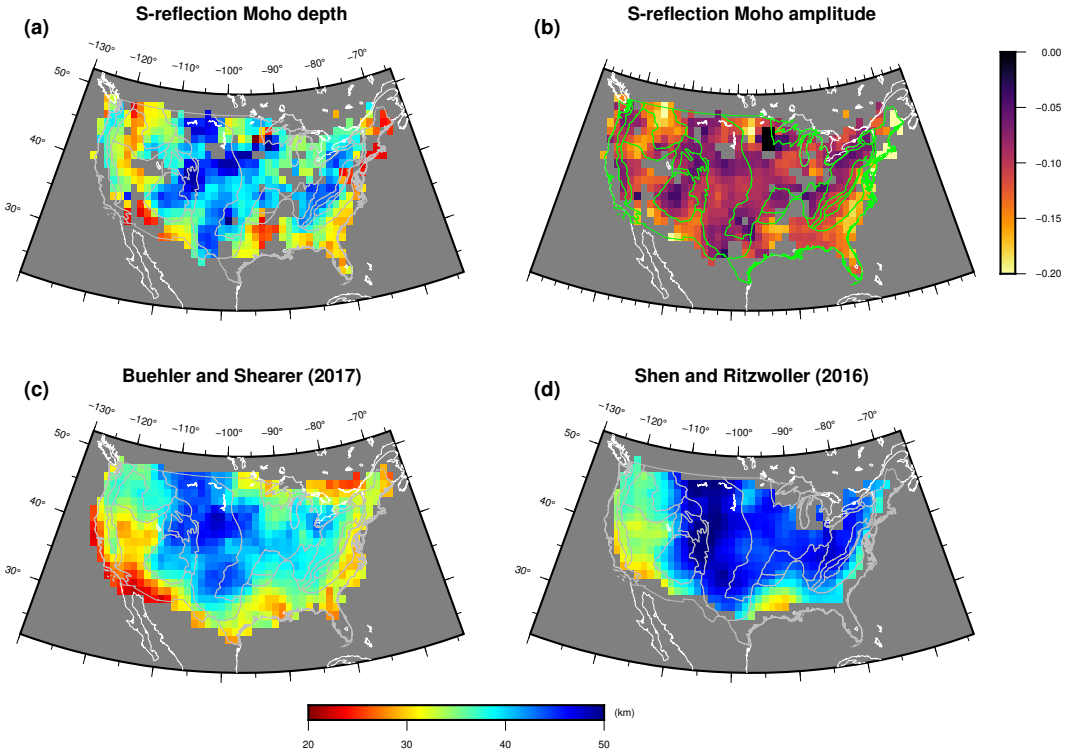

Figure 7. Comparison between our Moho observations and previous studies. (a) and (b) Moho depth and amplitude, respectively, from our CRP image (c) Moho depth from Buehler and Shearer (2017). (c) Moho depth from Shen and Ritzwoller (2016).

of Buehler and Shearer (2017), and (2) the joint surface-wave and PRF inversion of Shen and Ritzwoller (2016). The maps show reasonable agreement, particularly for the largest-scale features, which gives us some confidence that our method is capable of mapping shallow reflectors. However, we defer more detailed study of crustal structure for future work, preferring to focus here on imaging lithospheric structure, where our approach has perhaps its greatest potential advantages over other imaging methods.

3.3 Lithospheric discontinuities

On our S-reflection images, the mantle arrivals are predominantly positive (corresponding to NPRs) for both the Western US (WUS) and the Central and Eastern US (CEUS), though these arrivals appear stronger and more focused in the WUS than in the CEUS (Fig. 5a–f). In addition, we do not observe any NPR that extends across the whole continent, indicating that the NPRs in the WUS and the CEUS are likely unrelated features. Thus, we follow previous studies (e.g. Hopper and Fischer (2018)) to discuss our results in the WUS and CEUS separately.

3.3.1 The lithosphere-asthenosphere boundary in the Western US

In the WUS, we observe a clear NPR in the depth range of 60–110km on almost every trace of Profiles A1–A5 (yellow bars in Figs. 5a–e), which is clearly not due to Moho sidelobes because the Moho is generally shallow (< 40km) in the WUS. Since most previous studies using SRFs also showed a negative interface in this depth range, which was commonly interpreted as the LAB in the WUS (e.g. Hopper and Fischer (2018), L. Liu and Gao (2018), and Kind et al. (2020)), we adopt their interpretation and search for

the strongest local maxima in the depth range of 60–110km in our CRP image volume to evaluate the depth and amplitude variation of the LAB in the WUS. In areas where the Moho is deep and the negative peak immediately below the Moho is strong, e.g., the Colorado Plateau, this automatic picking algorithm identifies the negative peak directly below the Moho as the LAB. In such cases, we manually move the LAB picks to a deeper NPR when this deeper NPR is also in the depth range of 60–110km, has similar amplitude to the one directly below the Moho, and appears horizontally continuous. We note that strong positive arrivals are present above our LAB and sometimes directly beneath the Moho in some areas (e.g. beneath the Colorado Plateau; Fig. 5c), which cannot be explained with Moho sidelobes alone due to their high amplitudes and thus likely represent NPRs within the lithosphere. However, since these NPRs do not appear to be spatially prevalent, we will focus on the LAB in this study while deferring detailed discussion of these shallow NPRs to future studies.

On our LAB depth and amplitude map (Fig. 8), we observe a strong and shallow ($<$ 70km) LAB in the following regions: (1) The area that covers the eastern Colorado Plateau, the southern Rocky Mountains, and the Rio-Grande Rift; (2) The northern Rocky Mountains; (3) The Wasatch Fault Zone, which marks the transition zone between the northern Basin and Range Province and the middle Rocky Mountains; and (4) The Sierra Nevada Transition Zone. Although in some of these areas the LAB is picked at the negative peak immediately below the Moho, we find them to be appropriate LAB picks because they appear to be the continuations of the LAB at greater depths in adjacent areas. An example of such cases is the LAB below the Wasatch Fault Zone ($\sim$ 111°W on Profile A3), where the NPR at $\sim$ 70km clearly represents the end of the eastward shallowing trend of the LAB between $\sim$ 116°W and $\sim$ 111°W. The LAB in the northern Basin and Range Province and the Cascade Arc is also strong but at moderate depth ($\sim$ 90km). In the Columbia Plateau, the LAB is weaker than in the adjacent Cascade Arc but at similar depth, whereas the LAB in the southern Basin and Range Province is both weaker and deeper than the northern Basin and Range Province. The LAB in the Wyoming Basin is also deep and weak.

Since the free-surface-Moho double reflection (hereafter "Moho double reflection") has a positive polarity and arrives at a similar time window to our LAB (Fig. 1), it might be misidentified as the LAB. To assess this possibility, we plot the Moho depth and amplitude against the LAB depth and amplitude for each grid point in the WUS, and find little correlation (Figs. 9a, b), making it unlikely that our LAB observations are caused by Moho double reflections.

We note that the depth variations of our LAB in Figure 8 do not agree very well with the depth maps of negative-velocity-gradient features in the WUS previously obtained from SRF studies (e.g., Figure 3 from L. Liu and Gao (2018) and Figure 5 from Hopper and Fischer (2018)). We focus here on comparisons to Hopper and Fischer (2018) and plot a depth and amplitude comparison obtained by averaging the LAB depths and amplitudes from Hopper and Fischer (2018) within our grid cells (Fig. S3). The SRF LAB is generally shallow ($<$ 80km) in the Basin and Range Province, the Columbia Plateau, and the northern Rocky Mountains, and deep in the Colorado Plateau ($>$ 90km), which is very different from our LAB depth distribution. Perhaps the only clear similarity between our LAB depth and the SRF results is the shallow LAB in the Wasatch Fault Zone and the Sierra Nevada Transition Zone. The SRF LAB amplitude generally lacks strong variations, with a slightly stronger LAB in the Basin and Range Province and the northern Rocky Mountains, which is also different from our LAB amplitude distribution. In summary, the characteristics of our inferred LAB in the WUS appear significantly different from the LAB results of Hopper and Fischer (2018).

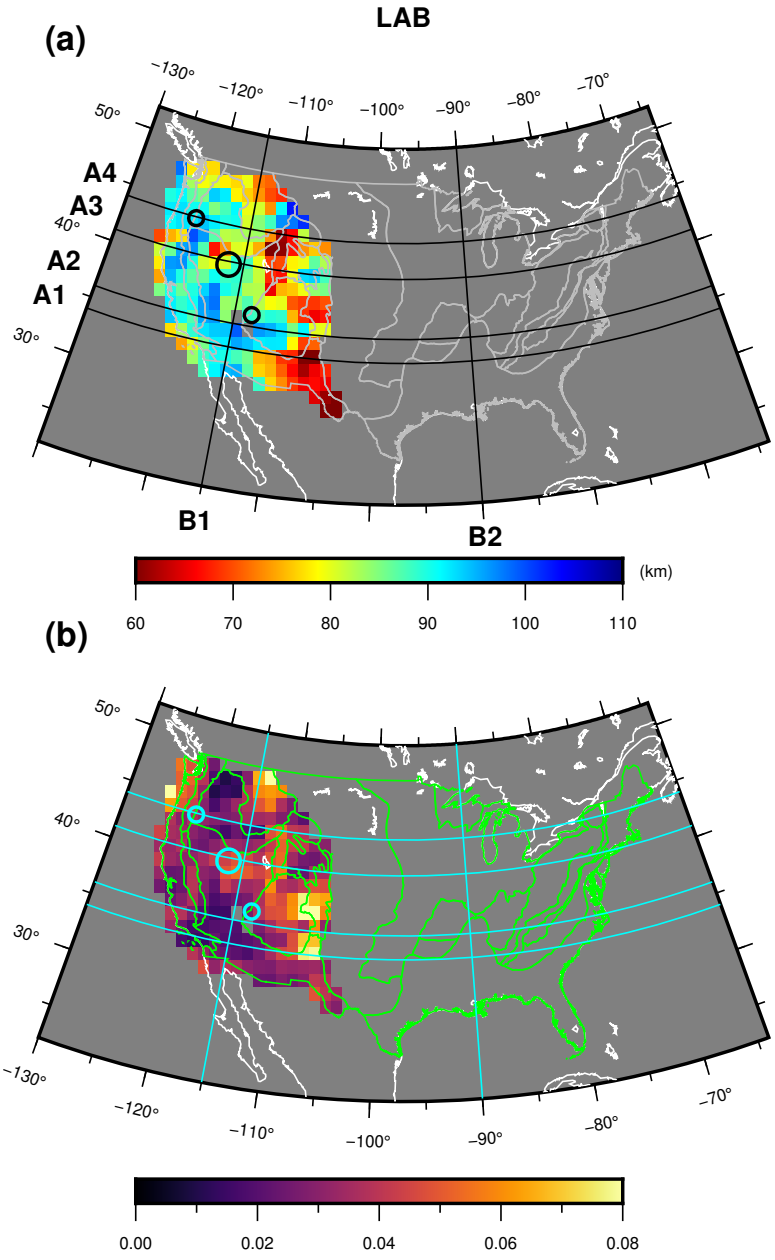

Figure 8. Comparison between the depth and amplitude of our imaged LAB and results from Hopper and Fischer (2018). (a) and (b): Our LAB depth and the SRF-inferred LAB depth from Hopper and Fischer, respectively. (c) and (d): Our LAB amplitude and that of Hopper and Fischer, respectively. Black and cyan circles in (a) and (c) mark the locations and sizes of the caps whose waveform stacks are modeled in Fig. 13. SNTZ: Sierra Nevada Transition Zone; WFZ: Wasatch Fault Zone.

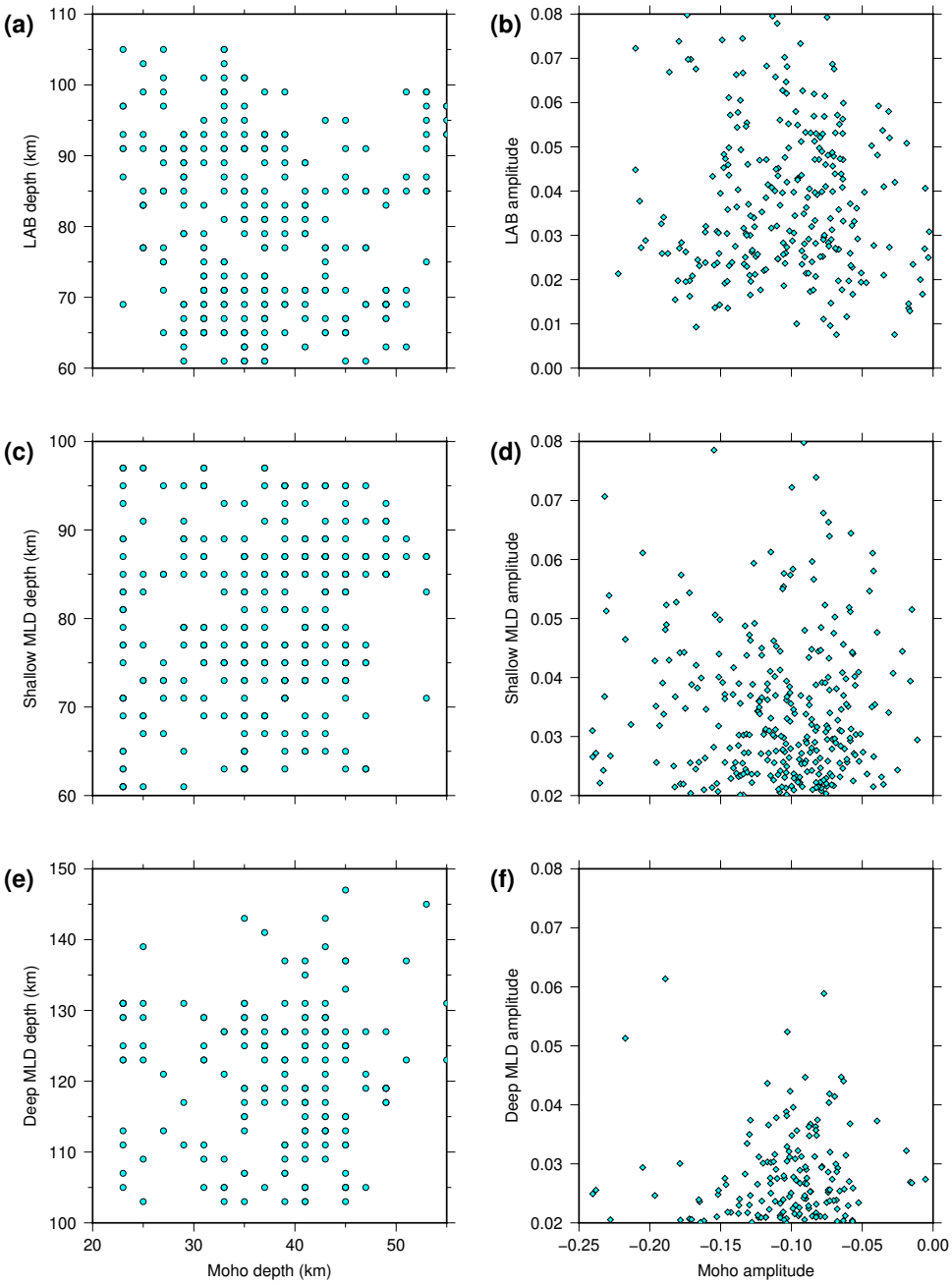

Figure 9. Cross plots of Moho amplitude and depth against the amplitude and depth of the LAB in the WUS and the MLDs in the CEUS. (a) Moho and LAB depth in the WUS. (b) Moho and LAB amplitude in the WUS. (c) Moho and shallow-MLD depth in the CEUS. (d) Moho and shallow-MLD amplitude in the CEUS. (e) Moho and deep-MLD depth in the CEUS. (f) Moho and deep-MLD amplitude in the CEUS.

3.3.2 Mid-lithospheric discontinuities in the Central and Eastern US

In the CEUS, despite the widespread positive arrivals in the mantle, none of these arrivals appear as spatially coherent as the LAB in the WUS. In addition, we often observe multiple positive arrivals with similar amplitude at different depths in some areas (e.g. $\sim 85°$W on Profile A2). To address this issue, we divide our image volume beneath the CEUS into two depth ranges: the Moho to 100 km depth and 100–150 km depth. We then find the maximum local maxima on each trace in each depth range and term them the shallow MLD and the deep MLD, respectively, because these NPRs appear to be within the high-velocity lithosphere shown by seismic tomography studies in the CEUS (e.g. H. Zhu et al. (2017)). Since the MLDs in the CEUS are generally weaker than the LAB in the WUS (Fig. 10c, d and 8b), and the CEUS generally has poorer data coverage than the WUS (Fig. 5g), we only show MLD depths at grid points with MLD amplitude > 0.02, which we regard as reliable picks (Fig. 10a, b). Since the depth range for the shallow MLD also contains Moho sidelobes, we assume that the shallowest positive arrival always represents the Moho sidelobe and ignore it while picking the shallow MLD. If the only positive arrival with amplitude > 0.02 between the Moho and 100 km depth is within 30 km of the Moho, we define it as the shallow MLD if its amplitude is greater than half of the local Moho amplitude, which indicates that it likely represents the superposition of an NPR and the Moho sidelobe. Although we define our two MLDs based on their depth ranges, we do not preclude the possibility that they may represent the same interface in some areas. For example, on Profile B2, the two MLDs may be two parts of one interface that dips southward between 35° and 45°N (Fig. 5f). Since our data coverage in the CEUS is usually insufficient for us to determine if our two MLDs are spatially connected, we will treat them as separate features in this study, while leaving discussions of their detailed geometries to future studies.

Our results show that the shallow MLD generally has a higher amplitude than the deep MLD, with the amplitude of both MLDs varying greatly across the CEUS (Fig. 10c, d). The amplitude of the shallow MLD is high in two main regions: (1) The northern Midcontinent Rift and (2) the southern Appalachian Mountains (Fig. 10c). In both areas the shallow MLD is ~ 85km deep (Fig. 10a). The deep MLD has strong amplitudes in three main regions: (1) The southern Midcontinent Rift; (2) the southern Appalachian Mountains; and (3) the area around Lake Erie (Fig. 10b). The deep MLD is ~ 125km deep beneath the southern Midcontinent Rift, ~ 115km deep beneath the southern Appalachian Mountains, and ~ 105km deep beneath the southern Appalachian Mountains. We also plot the depth and amplitude of our MLDs against the Moho depth and amplitude for every grid point with reliable observations in the CEUS, and find little correlation (Figs. 9c–f), indicating that our MLD observations are unlikely due to Moho sidelobes or Moho double reflections. Interestingly, our shallow and deep MLDs appear to have strong amplitudes in the same (e.g. the southern Appalachian Mountains) or adjacent regions (e.g. the southern and northern Midcontinent Rift), which implies that the two MLDs may be related features. We will further discuss this possibility in Section 4.4.

In the CEUS, our shallow MLD is in the same depth range as the maximum negative-velocity gradient (NVG) from Hopper and Fischer (2018), which was interpreted as an MLD in the Central US and the LAB in the Eastern US, and may represent the same interface. We thus compare the amplitude and depth distribution of our shallow MLD with those from Hopper and Fischer (2018) averaged within our grid cells (Fig. S4). The amplitude of the SRF NVG is generally uniform, in contrast to the strong amplitude variation of our shallow MLD (Fig. S4c, d). In the two areas where we observe strong shallow MLDs, the SRF NVG is at approximately the same depth as our MLD beneath the northern Midcontinent Rift but at significantly different depth from our MLD in the southern Appalachian Mountains (Fig. S4a, b). We note that although the northern Midcontinent Rift (which overlaps with most of the Superior Craton in the CEUS) does not show

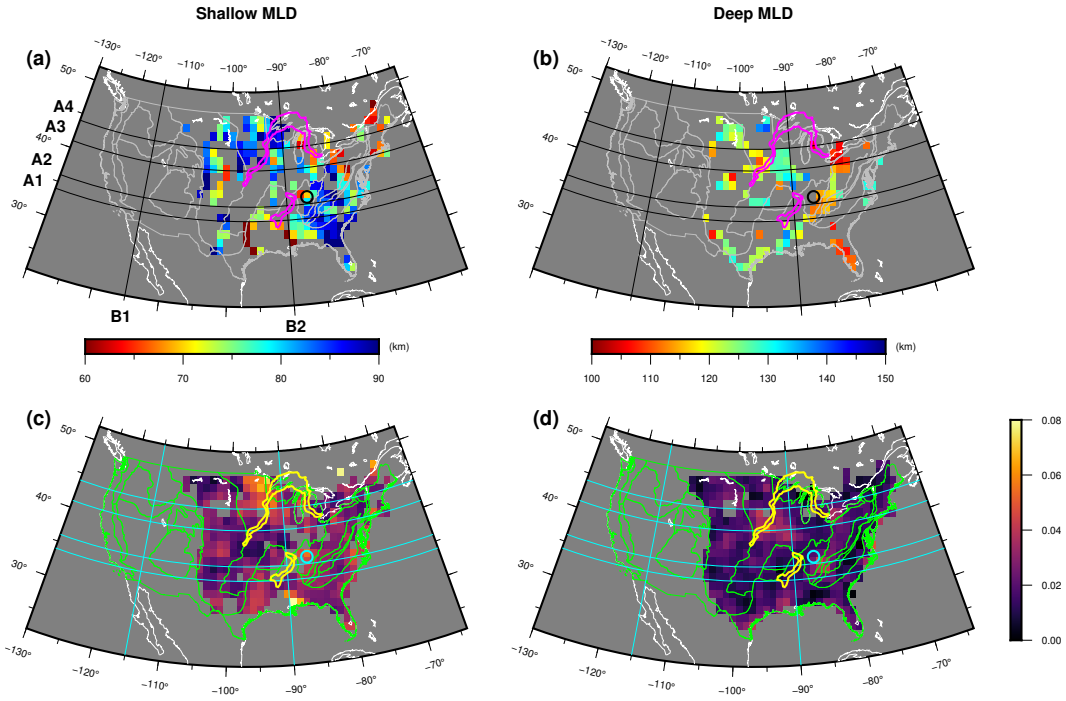

Figure 10. Depth and amplitude maps of our near-Moho MLD and deep MLD in the CEUS. (a) and (b): Depth maps of our near-Moho MLD and deep MLD in the CEUS, respectively. Only grid points with MLD amplitude > 0.02 are shown in (a) and (b), respectively. (c) and (d): Amplitude maps of our near-Moho MLD and deep MLD in the CEUS, respectively.

significantly larger SRF NVG amplitudes in Fig. S4d, Hopper and Fischer (2018) indeed found that this area has stronger and more spatially coherent MLD than most other parts of the CEUS. Thus, our results appear to agree with the SRF results from Hopper and Fischer (2018) for the MLD beneath the northern Midcontinent Rift.

4 Discussion

4.1 Comparison with PRF results

Although PRF and SRF have similar sensitivity to elastic parameter changes across discontinuities, studies of lithospheric discontinuities using PRF and SRF have not always yielded consistent results (e.g. Levander and Miller (2012) and Hansen et al. (2015)). As discussed above, although we observe NPRs within a similar depth range to those seen in SRF studies, the depths and locations of specific features do not agree very well. Some of these differences may be related to the broader depth resolution of the SRF compared to our S-reflection method, so it is worthwhile also comparing our images with PRF results, which should have depth resolution closer to our images than that of SRFs. Thus, we compare our S-reflection CRP images with our PRF CCP images along our four W-E profiles A1–A4 and two S-N profiles B1 and B2 (Figs. 11 and 12). To estimate the depth range where we expect the interference of Moho *PpPs*, we also compute the predicted depths of Moho *PpPs* for each trace using the local Moho depth and an average crustal V_p/V_s ratio of 1.73 (gray diamonds in Figs. 11 and 12).

We observe good agreement between the variation trend of the S-reflection Moho depth and PRF Moho depth along all the profiles, though the absolute Moho depth can be off by up to 10km (Figs. 11 and 12), likely because we did not account for variations

in average crustal V_p/V_s ratio (both our S-reflection and PRF images are computed using the IASP91 model). The PRF traces show sharper Moho arrivals and more detailed crustal structures because the PRFs are filtered at much higher frequency than our S reflection traces. Below the Moho, our PRF images also show similar features to our S-reflection images in many areas. On Profile A1, both the S-reflection and PRF images show clear negative interfaces between 50 and 90km beneath the southern margin of the Colorado Plateau and the Rio-Grande Rift, which we interpret as the S-reflection LAB beneath the region (Fig. 11a). We also observe negative interfaces at $\sim$ 75km depth beneath the Appalachian Mountains on Profile A1 of both methods, which we interpret as the shallow S-reflection MLD (Fig. 11a). On Profile A2, the multiple negative interfaces beneath the Colorado Plateau appear very consistent between the S-reflection and PRF images, which includes our S-reflection LAB. In addition, similar to Profile A1, both S-reflection and PRF images show negative interfaces below the Appalachian Mountains on Profile A2, which includes both the shallow and deep S-reflection MLD in the area, though the PRF interfaces appear significantly weaker (Fig. 11b). On Profile A3, we observe negative interfaces between 60 and 90km depth beneath the Wyoming Basin on both the S-reflection and PRF images, which includes the S-reflection LAB and shallow S-reflection MLD (Fig. 11c). We also observe negative interfaces beneath the western foothills of the Appalachian Mountains between 80 and 100km depth on Profile A3 of both methods, which is interpreted as the shallow S-reflection MLD (Fig. 11c).

Moving further north, on Profile A4, both the S-reflection and PRF images show clear sub-horizontal negative interfaces beneath the Cascade Arc and the Columbia Plateau, though the interface on the PRF image appears significantly shallower east of 123°W. Since the PRF interface is significantly broader west of 123°W than to the east, this apparent discrepancy between the two methods might be because the eastward shallowing Moho *PpPs* arrival (gray diamonds in Fig. 11d) and possibly also the reflection at the interface of the Juan de Fuca Plate, both of which are negative arrivals, cancel the bottom part of the broad negative PRF interface and make the interface appear shallower (Fig. 11d). Similar to Profile A1–A3, on Profile A4, we observe negative interfaces beneath the Appalachian Mountains between 60 and 90km on both our S-reflection and PRF images (Fig. 11d), which includes the shallow S-reflection MLD in this region. On Profile B1, the negative interface between 80 and 90km beneath the northern Basin and Range Province and northern Rocky Mountains, which is picked by us as the S-reflection LAB, appear very consistent between the S-reflection and PRF images (Fig. 12a). The broad negative S-reflection interface beneath the northern Rocky Mountains on this profile likely includes both the PRF interfaces at $\sim$ 80km and $\sim$ 60km depths (Fig. 12a). The similarity between the S-reflection and PRF image on Profile B2 is not as obvious as on the other profiles, but the two images still agree on the presence of negative interfaces beneath the Midcontinent Rift in the depth range of 60–90km (Fig. 12b), which we interpret as the shallow S-reflection MLD in this region.

Two main factors may contribute to the discrepancies between our S-reflection and PRF results. First and most importantly, Moho *PpPs* and the other Moho multiples could interfere with *Ps* from lithospheric discontinuities, which is also the primary reason that PRFs are less popular than SRFs in studying lithospheric structure. As shown in the above comparison between S-reflection and PRF results, the agreement between them is significantly better in the top 100km, a depth range generally free of the interference of Moho multiples (The first Moho multiple, Moho *PpPs*, is mapped to $>$ 100km depth on most traces; Figs. 11 and 12). In addition, multiples generated by intra-crustal interfaces may also interfere with *Ps* from lithospheric discontinuities (e.g. Fig. 1), though their effects should be less pronounced than the Moho multiples. Second, significant changes in anisotropy properties may be present at some lithosphere discontinuities, causing these discontinuities to have distinctly different behavior for S-reflections and PRFs. We will discuss the effects of anisotropy in more detail in Section 4.3.

The general agreement between our S-reflection and PRF images not only helps validate our methodology but also implies the potential of joint analyses between the two methods. Because lithospheric discontinuities are generally weak and subject to contamination from Moho multiples and other phases, the presence of a discontinuity on both S-reflection and PRF results is strong evidence for the existence of the interface. Moreover, since S-reflections and PRFs contain seismic responses for two independent systems, SH and P-SV, a joint analysis of them could better constrain the anisotropic properties of a discontinuity, though this analysis will require good event-azimuth coverage and may only be applied to depth ranges free of PRF Moho multiples (e.g. $<$ 100km for the contiguous US). In addition, jointly analyzing Moho S-reflections and Moho *Ps* could constrain the average crustal V_p/V_s ratio, a key parameter closely related to average crustal composition (Yuan, 2015; T. Liu et al., 2019), in a similar way to the classic $H-\kappa$ stacking technique (L. Zhu & Kanamori, 2000). A potential advantage of this method is that it does not rely on the PRF Moho multiples, which are not always reliably observed. The application of this analysis may require the S-reflection data to be filtered to higher frequency than used in this study, for example to a similar frequency band as typically used for SRF studies (Fig. 1), which would be more suitable for studying crustal structures.

4.2 Waveform modeling

To provide a more quantitative estimate of the size of the velocity drops at our LAB and MLDs discussed above, we perform waveform modeling on stacked S-reflection waveforms for four circular caps, three for the LAB in the WUS and one for the MLDs in the CEUS (locations and sizes of the caps are shown in Figs. 8, 10; waveforms are shown in Figs. 13–14). To address the uneven data coverage, we allow the radius of each cap to grow starting from 70 km, which is approximately the Fresnel Zone radius at 70 km depth for our data, until the cap includes more than 100 reflection points at 70 km depth. We then choose $\pm$20s of the stacked trace as the reference pulse and follow the ray-theoretical inversion procedure in Shearer (1996) to derive a 1D velocity and density model for each cap. Since the methods in Shearer (1996) does not account for the effects of multiple reflections, whereas the Moho double reflections may interfere with our NPR signals, we compute synthetic waveforms with our velocity and density models using the reflectivity method from Kennet (2009), which automatically includes all possible reflection phases (blue waveforms in Figs. 13–14). To evaluate the effects of Moho double reflections on our waveform fitting, we also compute synthetic waveforms with no free-surface multiples (only one reflection is allowed at the free surface) by including only the leading two terms of Equation 6.17 in Kennet (2009) for the free surface reflection (cyan waveforms in Figs. 13–14). We also compute synthetic waveforms using our models with all mantle velocity variations removed (dark gray waveforms in Figs. 13–14) to further test if these variations are required to produce key features of our observed waveforms. When deriving the velocity and density models from the observed waveforms, we assume that the density is at a fixed ratio to the velocity across the whole model so that we only need to solve for the velocity profile (Shearer, 1996). Therefore, in our models, the density also drops when the velocity drops with depth, which might not be physically realistic due to gravitational instability. If we reduce the density drops associated with the velocity drops in our models, more velocity reduction will be required to produce the same signal amplitude because the amplitude of an SH reflection is mostly determined by the impedance contrast across the interface. We recognize these limitations of our waveform modeling procedure and treat its results only as preliminary estimates of the velocity drops required to explain our NPR observations.

We first model the waveforms for three caps in the Cascade Arc, the northern Basin and Range Province, and the western Colorado Plateau, respectively (Fig. 8), which are examples for the LAB in the WUS. Our estimated velocity models show the Moho at similar depths as the average velocity model of Shen and Ritzwoller (2016) for each cap but very different mantle velocity profiles from Shen and Ritzwoller (Fig. 13). For the

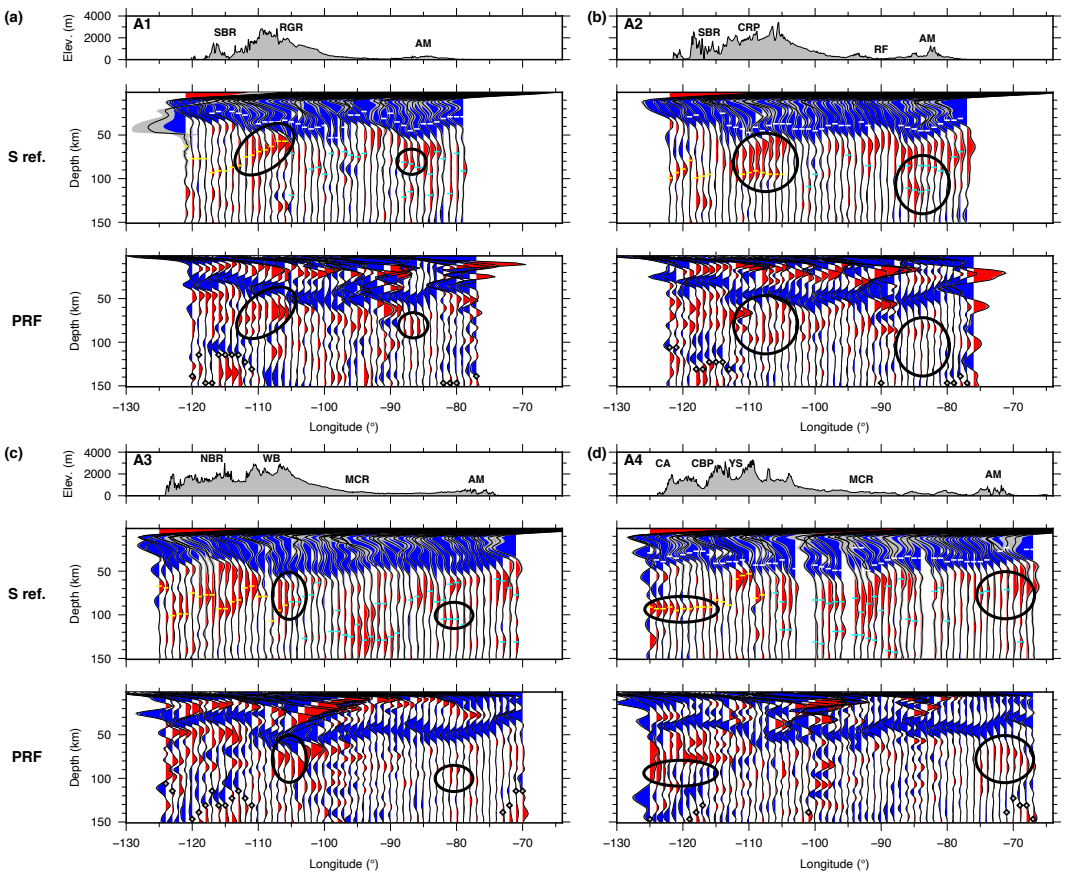

Figure 11. Comparison between our S-reflection results and our PRF common-conversion-point (CCP) image computed with the EARS PRFs along Profiles A1–A4. On both the S-reflection and the PRF traces, blue indicates velocity or impedance increasing with depth and red indicates velocity or impedance decreasing with depth. The parts of the profiles where S reflections and PRFs show similar structures are marked in black. Gray diamonds: predicted depths of Moho *PpPs*. The interface markers and acronyms of key tectonic features are the same as in Fig. 5

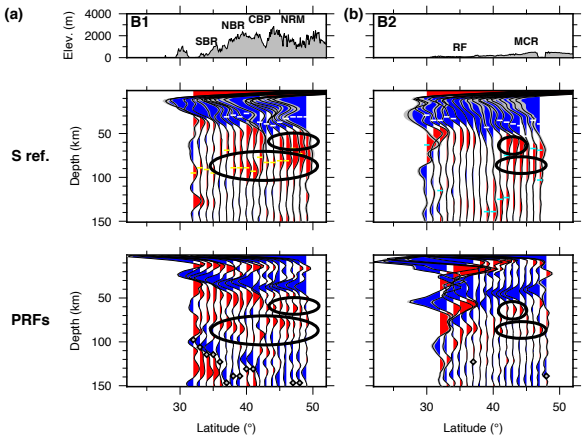

Figure 12. The same as Fig. 11, but for Profiles B1 and B2.

Cascadia cap, the LAB reflection requires a V_s drop of $\sim 7\%$ over ~ 10km at ~ 90km depth (Fig. 13a). The synthetic waveform without free-surface multiples does not differ significantly from the one with multiples (Fig. 13a) likely due to the weak Moho reflection in this cap. For the northern-Basin-and-Range cap, the LAB reflection requires a V_s drop of $\sim 6\%$ over ~ 10km at ~ 90km depth (Fig. 13b), though this velocity drop is followed by a few smaller velocity drops at greater depth, which might be due to the minor positive arrivals after the LAB reflection (Fig. 13b). The negative velocity gradient consisting of all these velocity drops spans a broad depth range of over 50 km, in which the velocity decreases by $\sim 20\%$. For this cap, the synthetic waveform without free-surface multiples has a stronger LAB reflection because the negative trailing sidelobe of the Moho double reflection (dark gray waveform in Fig. 13) reduces the amplitude of the LAB reflection. For the Colorado-Plateau cap, the LAB signal requires a V_s drop of $\sim 7\%$ over ~ 20km at ~ 90km depth (Fig. 13c). The synthetic waveform without free-surface multiples has a LAB reflection slightly weaker than the one with multiples, likely because the Moho double reflection in this case, though weak, arrives almost at the same time as the LAB reflection and enhances its amplitude (Fig. 13c). For all three caps, the synthetic waveforms computed with no mantle velocity variations (dark gray waveforms in Fig. 13) clearly fail to produce the LAB reflections shown by our observed waveforms, indicating that the velocity drops are required to explain our observations. The three caps presented here are regions where the LAB reflection is moderately strong, which could provide a reference for first-order estimations of velocity drops at regions with significantly stronger (e.g. the Rio-Grande Rift) and weaker (e.g. the southern Basin and Range Province) LAB reflections (Fig. 8c).

The MLDs in the CEUS are usually characterized by multiple peaks at different depths with similar amplitude (Figs. 5a–f), which often cannot be modeled appropriately with our simple inversion scheme. We thus only model the waveform stack of one cap in the southern Appalachian Mountains close to the Reelfoot Rift (black and cyan circles in Fig. 10), which is dominated by the strong reflection at the shallow MLD. For this cap, our model gives a very similar Moho depth as that of Shen and Ritzwoller (2016) but shows a significant negative velocity gradient immediately below the Moho spanning the depth range 60km–110km, which is not included in the model of Shen and Ritzwoller (Fig. 14). In this layer, the velocity gradient gradually decreases with depth, with $\sim 8\%$ velocity reduction in the top 20km and $\sim 15\%$ velocity reduction across the whole layer (Fig. 14). For this cap, because the MLD is immediately below the Moho, the MLD reflection arrives at almost the same time as the Moho sidelobe (Fig. 14). However, the positive peak following the Moho reflection on the observed waveform (black waveform in Fig. 14) is significantly stronger than the synthetic waveform computed with a constant mantle velocity (dark gray waveform in Fig. 14), whereas the synthetic waveforms computed with the model including the negative velocity gradient (blue and cyan waveforms in Fig. 14) clearly fit the observed waveform better. The two synthetic waveforms computed with the models including the negative velocity gradient show similar amplitude for the MLD reflection because the Moho double reflection is weak and arrives much later than the MLD arrival. Since the southern Appalachian Mountains is among the areas with the strongest MLD reflections (Figs. 10c, d), the velocity drop shown in this example can be treated as an upper limit for velocity drops at the MLDs in the CEUS.

4.3 Nature of the LAB and its relation with active tectonics in the Western US

Our LAB amplitude varies greatly across the WUS. In areas where the LAB is strong, e.g., the Cascade Arc, the northern Basin and Range Province (Fig. 8c), and the Colorado Plateau, the velocity drop at the LAB ($\sim 7\%$ over ~ 15km) is clearly too large to be explained with thermal effects alone, which could at most generate a $\sim$ 8% velocity drop over 65km (Hopper & Fischer, 2018). In areas where the LAB is weak, e.g., the southern Basin and Range Province and the Columbia Plateau (Fig. 8c), thermal

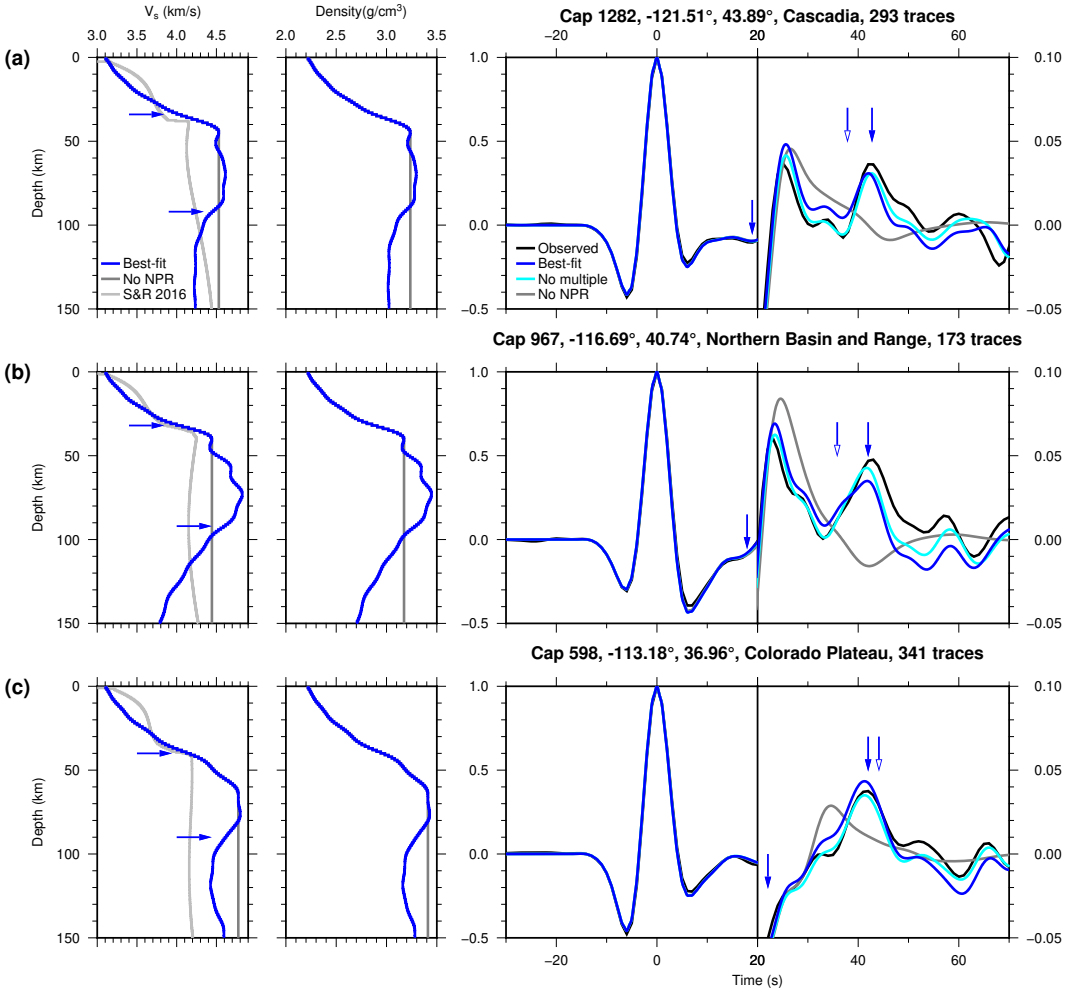

Figure 13. Waveform modeling for three caps in (a) the Cascade Arc, (b) the northern Basin and Range Province, and (c) the Colorado plateau (Fig. 8) as examples for velocity contrast at the LAB in WUS. Black curve: Stack of the observed waveforms in the cap. Blue models and waveforms: Our preferred models and the waveforms computed with them using a reflectivity algorithm that includes free-surface multiples (including Moho multiples). Cyan waveforms: Waveforms computed with our preferred model but a reflectivity algorithm that excludes free-surface multiples. Dark gray models and waveforms: Models derived by retaining only crustal velocity and density variation in our preferred models and the waveforms computed with them using a reflectivity algorithm that includes free-surface multiples. Light gray models: Averaged V_s model from Shen and Ritzwoller (2016) for each cap. Solid arrows in each velocity profile mark the depth of the Moho and the LAB, which are used to compute the arrival times of the Moho and LAB reflections marked with solid arrows in the waveform panels. Empty arrows mark the arrival times of the first Moho multiple. The locations and sizes of the caps are shown in Fig. 8

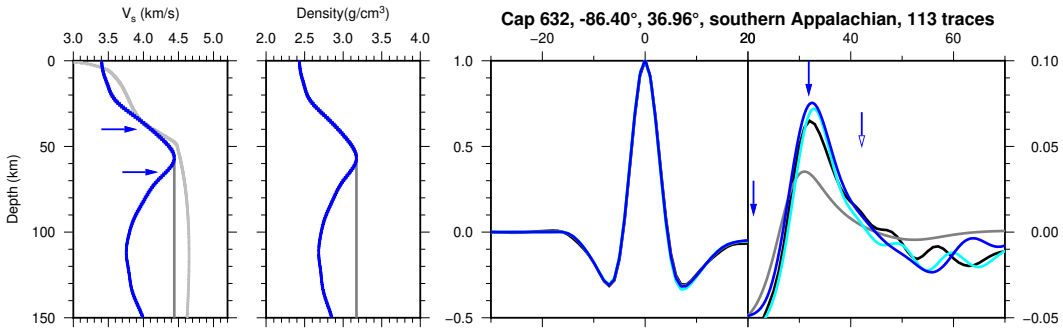

Figure 14. Same as Fig. 12, but for a cap in the southern Appalachian Mountains as an example for velocity contrast at MLDs. The location and size of the cap is shown in Fig. 10

effects might be sufficient to generate the LAB signals, though a more detailed analysis of the waveforms and the local thermal structure is required to evaluate this hypothesis. However, in some areas with a weak LAB, e.g., the southern Basin and Range Province, we sometimes observe a significantly deeper reflector at $\sim$ 130km with similar or higher amplitude than the LAB (yellow circles in Figs. 5c–e), which may represent a sharper velocity drop than the local LAB and thus cannot be explained with thermal effects alone. In summary, mechanisms other than purely thermal effects are likely responsible for the LAB and associated features in the WUS.

A mechanism commonly invoked to explain the LAB beneath oceans and young continents is the presence of a small amount of partial melt at the base of plates, which could effectively reduce V_s and generate the sharp arrivals on scattered-wave observations (e.g. Rychert et al. (2020), Hopper and Fischer (2018), and Kawakatsu et al. (2009)). Since our observed velocity drop at the LAB is similar to those from previous studies that explained their LAB observations with the presence of partial melt (e.g. Hopper and Fischer (2018)), this mechanism could also explain our LAB observations. However, when partial melt is present at the base of tectonic plates, the melt will tend to segregate into sub-horizontal melt-rich shear bands due to the relative motion between the plates and the underlying asthenosphere (B. Holtzman et al., 2003; Katz et al., 2006), causing $V_{SH} > V_{SV}$ in the layer that constitutes the LAB (B. K. Holtzman & Kendall, 2010; Kawakatsu et al., 2009). The anisotropy of this layer will produce a significantly larger drop in V_{SV} than V_{SH} at the LAB and thus generate a stronger signal on receiver functions, which are sensitive to V_{SV} changes, than S reflections, which are sensitive to V_{SH} changes. This prediction is inconsistent with our observations of a strong S-reflection LAB in many areas. However, this model may explain why some areas appear to have strong negative converters below the Moho on PRF images but lack corresponding features on S-reflection images, e.g., the southern Basin and Range Province (Figs. 11a, b and 12a). To characterize the nature of the LAB in the WUS clearly requires further analyses combining multiple seismic observations, which is beyond the scope of this study.

The characteristics of our LAB observations show clear correlation with tectonic features in the WUS. Perhaps the best example of this correlation is the shallowing of the LAB at the western and eastern boundaries of the northern Basin and Range Province (Figs. 5b and 8a), which is consistent with GPS observations that extension in the northern Basin and Range Province is mostly happening on its eastern and western boundaries (e.g. Hammond et al. (2014), Thatcher et al. (1999), Martinez et al. (1998)). In particular, Thatcher et al. (1999) and Martinez et al. (1998) found concentrated extension at the Sierra Nevada Transition Zone and the Wasatch Fault Zone, where we also observe significant lithosphere thinning (Figs. 5b and 8a). Interestingly, the lithospheric thickness in the northern Basin and Range Province seems to be inversely correlated with

the crustal thickness, which is greater near the edges than in the center (Figs. 5b and 7a, b). If we regard the crustal thickness in the northern Basin and Range Province as a measure of cumulative past lithosphere extension, this suggests that active tectonic processes, as opposed to past ones, likely control the characteristics of the LAB in the WUS. This dynamic model of the LAB is consistent with the strong observed variations in both LAB depth and amplitude across the WUS, where different regions are undergoing diverse tectonic processes.

4.4 Existence of MLDs in the Central and Eastern US

The existence of MLDs in the Central US is much debated, with different SRF studies presenting varying results. Using similar techniques, Hopper and Fischer (2018) and L. Liu and Gao (2018) agreed that an MLD is present in the depth range of 70–100km in the Central US. In contrast, Kind et al. (2020) argued that the MLD in the Central US shown in Hopper and Fischer (2018) and L. Liu and Gao (2018) is largely an artifact caused by the Moho sidelobe. The shallow MLD in our results is approximately in the same depth range as the MLD from the SRF studies (Hopper & Fischer, 2018; L. Liu & Gao, 2018) and thus might represent the same interface. However, our shallow MLD shows strong amplitude variation and may only exist in spatially isolated areas, unlike the nearly ubiquitous MLD shown by previous SRF studies (Hopper & Fischer, 2018; L. Liu & Gao, 2018). Since our MLD has high amplitude in areas where Hopper and Fischer (2018) found stronger and more spatially coherent MLDs (e.g. the northern Midcontinent Rift), this discrepancy between our results and previous SRF results could at least be partly due to the significantly lower depth resolution of SRFs compared with S reflections. In summary, our results confirm the presence of MLDs in the CEUS but suggest that they are likely regional as opposed to continental-scale features.

The two areas in the CEUS where we observe strong shallow and deep MLDs, the Midcontinent Rift and the southern Appalachian Mountains, both underwent major past tectonic processes, which implies that the MLDs in the CEUS may be closely related to past episodes of intensive lithosphere deformation. In the Midcontinent Rift, the shallow and deep MLD may represent different parts of a south-dipping interface (Fig. 5f), which is associated with the Proterozoic rifting process. In the southern Appalachian, where previous studies have uncovered the crustal suture of the Appalachian Orogeny (Hopper et al., 2017), the MLDs that we observe may represent features associated with the mantle suture. Since the CEUS is generally less well sampled by our dataset compared with the WUS (Fig. 5g), future studies incorporating data from local temporary arrays are needed to uncover more details of the MLDs in the CEUS, especially in the areas with strong evidence of their presence, e.g., the Midcontinent Rift and the southern Appalachian Mountains.

4.5 How can we best resolve lithospheric structure?

Here, we introduce a new method for imaging lithospheric structure that analyzes topside multiples from teleseismic SH waves generated by deep earthquakes, and apply it to data from TA and other networks in the contiguous United States. The use of deep earthquakes removes the ambiguity between source- and receiver-side lithospheric reflections that complicated the earlier TA study of Shearer and Buehler (2019). Our new approach indeed produces images significantly different from Shearer and Buehler (2019). For example, our LAB in the WUS has a very different depth distribution from the NPR shown in Figure 10 of Shearer and Buehler (2019), which was picked in a similar depth range as our LAB. We believe that our results about lithospheric discontinuities are superior to those from Shearer and Buehler (2019) because our new approach significantly reduces artifacts due to the source-receiver ambiguity in Shearer and Buehler (2019). Our method has similarities to standard reflection seismology techniques, including common-reflection-point stacking. However, the distribution of deep earthquakes is much sparser,

particularly in azimuth, than the source distribution of typical controlled-source reflection experiments, which reduces the robustness of our results. Thus, although we use the term "image" throughout this paper to refer to reflectors defined by peaks in the waveform stacks, some caution is warranted because some of these features might be artifacts caused by scattering from 3D structures more complex than the simple horizontal layering that common-reflection-point stacking implicitly assumes. This is also a concern for receiver-function methods, which also generally suffer a non-uniform source distribution. Note that the uncertainty introduced by possible scattered arrivals is distinct from the question of the statistical significance of the peaks in the waveform stacks, which can be assessed using bootstrap resampling or other methods. These formal statistical uncertainties generally become quite low when the stacking fold is large, but this does not address the issue as to whether the seismic waves generating a peak are coming from the assumed common-reflection-point (or common-conversion-point) region or somewhere else.

Ideally, these imaging uncertainties could be reduced through more advanced reflection seismology methods, such as migration, but these methods perform best with uniform source and receiver distributions, which are difficult to achieve with natural seismicity and most existing seismic networks. Given these limitations, how can we best assess the reliability of our results for lithospheric structure? A reasonable approach is to focus on those features that are seen in more than one type of analysis, i.e., our topside reflection approach compared to P- and S-receiver functions. In this study, the best agreement between all three methods is seen in the largest scale features. For example, considering average continent-scale structures, the depth range between about 60 and 100 depth is characterized by velocity drops with depth that are strong enough to be imaged with all three methods (e.g. Fig. 6). This is seen for both the western and eastern United States and is a very consistent and robust result. However, as discussed above, at finer scales we find much better agreement between our results and PRF images than with SRF images. This discrepancy is somewhat surprising because SRFs are generally considered superior to PRFs for resolving lithospheric interfaces, as they are free of contamination from crustal multiples. However, as discussed earlier, a depth range exists below the Moho *Ps* and the earliest Moho reverberation Moho *PpPs* (Moho to $\sim$ 100km depth for the contiguous US), in which PRFs provide relatively clean images. It is also in this depth range that we observe the best agreement between our S-reflection and PRF profiles. We do not entirely understand why our results do not agree better with existing SRF results, but it is possible that the more limited depth resolution of SRFs compared to topside S reflections and PRFs (given the pulse frequencies and ray geometries involved) cause SRFs to be sensitive to different vertical scales.

Ultimately, there is a need for joint inversions that include both topside reflections and converted phases to exploit all the information in the upcoming teleseismic wavefield (e.g., Bostock et al. (2001), Kumar and Bostock (2006), Monteiller et al. (2015)). Not only could this provide more robust results for imaging interfaces, but also holds the potential to discriminate between different models for the changes in material properties at the interfaces, such as velocity drops caused by partial melt or changes in anisotropy strength or orientation. By combining data from multiple phases within both the P-SV and SH systems, it should be possible to obtain a more complete understanding of lithospheric structure than is possible from analyzing a single scattered or converted phase. Joint inversions of receiver functions with surface waves (e.g., Bodin et al. (2012), Julia et al. (2000), Shen et al. (2013)) have also proven useful by combining the power of surface waves to resolve large-scale absolute seismic velocities, albeit with limited depth resolution, and the sensitivity of body-wave converted and reflected phases to sharp velocity changes.

5 Conclusions

We construct high-resolution images of lithospheric discontinuities beneath the contiguous United States using teleseismic SH reflections from deep earthquakes as recorded by the Transportable Array and other regional seismic networks. In the western US, our results resolve the lithosphere-asthenosphere boundary at a depth between 60 and 110km, with characteristics that correlate well with active tectonic features in the area. In the Central and Eastern US, we observe two mid-lithospheric discontinuities in the depth ranges of 60–100km and 100–150km, respectively, which appear associated with past tectonic events. Our results show agreement with the results of P receiver functions in many regions, which implies the possibility of jointly constraining the properties of lithospheric discontinuities with both S-reflection and P-receiver-function observations.

Acknowledgments

This study is funded by NSF Grants EAR-1358510 and EAR-1829601. T.L. is supported by a Green Postdoctoral Scholarship. The data used in this study is freely available through the Incorporated Research Institutions for Seismology Data Management Center (IRIS DMC) https://ds.iris.edu/ds/nodes/dmc/. IRIS DMC is funded by the the NSF under Cooperative Support Agreement EAR-1851048. Data from the following seismic networks is used in this study: AE-Arizona Broadband SeismicNetwork; AG-Arkansas Seismic Network; BK-Berkeley Digital Seismograph Network; CC-Cascade Chain Volcano Monitoring; CI-Caltech Regional Seismic Network; CN-Canadian National Seismograph Network; CO-South Carolina Seismic Network; IE-INL Seismic Monitoring Program; IU-Global Seismograph Network; IW-Intermountain West Seismic Network; LD-Lamont-Doherty Lamont-Doherty Cooperative Seismographic Network; N4-Central and Eastern US Network; NC-USGS Northern California Regional Network; NE-New England Seismic Network; NM-Cooperative New Madrid Seismic Network; NN-Nevada Seismic Network; OH-Ohio Seismic Network; OK-Oklahoma Seismic Network; PE-Pennsylvania State Seismic Network; TA-Transportable Array; TX-Texas Seismological Network; US-United States National Seismic Network; UU-University of Utah Regional Seismic Network; UW-Pacific Northwest Seismic Network; WU-Southern Ontario Seismic Network; WY-Yellowstone National Park Seismograph Network. We thank Karen Fischer and Shun Ichiro-Karato for stimulating discussion.

References

Bodin, T., Sambridge, M., Tkalčić, H., Arroucau, P., Gallagher, K., & Rawlinson, N. (2012). Transdimensional inversion of receiver functions and surface wave dispersion. *Journal of Geophysical Research: Solid Earth*, *117*(B2).

Bostock, M., Rondenay, S., & Shragge, J. (2001). Multiparameter two-dimensional inversion of scattered teleseismic body waves 1. theory for oblique incidence. *Journal of Geophysical Research: Solid Earth*, *106*(B12), 30771–30782.

Buehler, J., & Shearer, P. (2017). Uppermost mantle seismic velocity structure beneath usarray. *Journal of Geophysical Research: Solid Earth*, *122*(1), 436–448.

Crotwell, H. P., & Owens, T. J. (2005). Automated receiver function processing. *Seismological Research Letters*, *76*(6), 702–709.

Fenneman, N. M. (1946). *Physical divisions of the united states* (Tech. Rep.). US Geological Survey.

Ford, H. A., Fischer, K. M., Abt, D. L., Rychert, C. A., & Elkins-Tanton, L. T. (2010). The lithosphere–asthenosphere boundary and cratonic lithospheric layering beneath australia from sp wave imaging. *Earth and Planetary Science Letters*, *300*(3-4), 299–310.

Hammond, W. C., Blewitt, G., & Kreemer, C. (2014). Steady contemporary deformation of the central basin and range province, western united states. *Journal of Geophysical Research: Solid Earth*, *119*(6), 5235–5253.

Hansen, S. M., Dueker, K., & Schmandt, B. (2015). Thermal classification of lithospheric discontinuities beneath usarray. *Earth and Planetary Science Letters*, *431*, 36–47.

Holtzman, B., Kohlstedt, D. L., Zimmerman, M. E., Heidelbach, F., Hiraga, T., & Hustoft, J. (2003). Melt segregation and strain partitioning: Implications for seismic anisotropy and mantle flow. *Science*, *301*(5637), 1227–1230.

Holtzman, B. K., & Kendall, J.-M. (2010). Organized melt, seismic anisotropy, and plate boundary lubrication. *Geochemistry, Geophysics, Geosystems*, *11*(12).

Hopper, E., & Fischer, K. M. (2018). The changing face of the lithosphere-asthenosphere boundary: Imaging continental scale patterns in upper mantle structure across the contiguous us with sp converted waves. *Geochemistry, Geophysics, Geosystems*, *19*(8), 2593–2614.

Hopper, E., Fischer, K. M., Wagner, L. S., & Hawman, R. B. (2017). Reconstructing the end of the appalachian orogeny. *Geology*, *45*(1), 15–18.

Julia, J., Ammon, C., Herrmann, R., & Correig, A. M. (2000). Joint inversion of receiver function and surface wave dispersion observations. *Geophysical Journal International*, *143*(1), 99–112.

Katz, R. F., Spiegelman, M., & Holtzman, B. (2006). The dynamics of melt and shear localization in partially molten aggregates. *Nature*, *442*(7103), 676–679.

Kawakatsu, H., Kumar, P., Takei, Y., Shinohara, M., Kanazawa, T., Araki, E., & Suyehiro, K. (2009). Seismic evidence for sharp lithosphere-asthenosphere boundaries of oceanic plates. *Science*, *324*(5926), 499–502.

Kennet, B. L. N. (2009). Seismic wave propagation in stratified media. In (chap. 6). Australian National University E Press.

Kennett, B., & Engdahl, E. (1991). Traveltimes for global earthquake location and phase identification. *Geophysical Journal International*, *105*(2), 429–465.

Kind, R., Mooney, W. D., & Yuan, X. (2020). New insights into the structural elements of the upper mantle beneath the contiguous united states from s-to-p converted seismic waves. *Geophysical Journal International*, *222*(1), 646–659.

Kumar, M. R., & Bostock, M. (2006). Transmission to reflection transformation of teleseismic wavefields. *Journal of Geophysical Research: Solid Earth*, *111*(B8).

Levander, A., & Miller, M. S. (2012). Evolutionary aspects of lithosphere discontinuity structure in the western us. *Geochemistry, Geophysics, Geosystems*, *13*(7).

Liu, L., & Gao, S. S. (2018). Lithospheric layering beneath the contiguous united states constrained by s-to-p receiver functions. *Earth and Planetary Science Letters*, *495*, 79–86.

Liu, T., Klemperer, S. L., Ferragut, G., & Yu, C. (2019). Post-critical sspmp and its applications to virtual deep seismic sounding (vdss)–2: 1-d imaging of the crust/mantle and joint constraints with receiver functions. *Geophysical Journal International*, *219*(2), 1334–1347.

Martinez, L. J., Meertens, C. M., & Smith, R. B. (1998). Rapid deformation rates along the wasatch fault zone, utah, from first gps measurements with implications for earthquake hazard. *Geophysical research letters*, *25*(4), 567–570.

Monteiller, V., Chevrot, S., Komatitsch, D., & Wang, Y. (2015). Three-dimensional full waveform inversion of short-period teleseismic wavefields based upon the sem–dsm hybrid method. *Geophysical Journal International*, *202*(2), 811–827.

Rychert, C. A., Fischer, K. M., & Rondenay, S. (2005). A sharp lithosphere–asthenosphere boundary imaged beneath eastern north america. *Nature*, *436*(7050), 542–545.

Rychert, C. A., Harmon, N., Constable, S., & Wang, S. (2020). The nature of the lithosphere-asthenosphere boundary. *Journal of Geophysical Research: Solid Earth*, *125*(10), e2018JB016463.

Rychert, C. A., & Shearer, P. M. (2009). A global view of the lithosphere-asthenosphere boundary. *Science*, *324*(5926), 495–498.

Savage, B., & Silver, P. G. (2008). Evidence for a compositional boundary within

the lithospheric mantle beneath the kalahari craton from s receiver functions. *Earth and Planetary Science Letters*, *272*(3-4), 600–609.

Shearer, P. M. (1991). Constraints on upper mantle discontinuities from observations of long-period reflected and converted phases. *Journal of Geophysical Research: Solid Earth*, *96*(B11), 18147–18182.

Shearer, P. M. (1996). Transition zone velocity gradients and the 520-km discontinuity. *Journal of Geophysical Research: Solid Earth*, *101*(B2), 3053–3066.

Shearer, P. M., & Buehler, J. (2019). Imaging upper-mantle structure under usarray using long-period reflection seismology. *Journal of Geophysical Research: Solid Earth*, *124*(9), 9638–9652.

Shen, W., & Ritzwoller, M. H. (2016). Crustal and uppermost mantle structure beneath the united states. *Journal of Geophysical Research: Solid Earth*, *121*(6), 4306–4342.

Shen, W., Ritzwoller, M. H., & Schulte-Pelkum, V. (2013). A 3-d model of the crust and uppermost mantle beneath the central and western us by joint inversion of receiver functions and surface wave dispersion. *Journal of Geophysical Research: Solid Earth*, *118*(1), 262–276.

Thatcher, W., Foulger, G., Julian, B., Svarc, J., Quilty, E., & Bawden, G. (1999). Present-day deformation across the basin and range province, western united states. *Science*, *283*(5408), 1714–1718.

Yuan, H. (2015). Secular change in archaean crust formation recorded in western australia. *Nature Geoscience*, *8*(10), 808–813.

Zhu, H., Komatitsch, D., & Tromp, J. (2017). Radial anisotropy of the north american upper mantle based on adjoint tomography with usarray. *Geophysical Journal International*, *211*(1), 349–377.

Zhu, L., & Kanamori, H. (2000). Moho depth variation in southern california from teleseismic receiver functions. *Journal of Geophysical Research: Solid Earth*, *105*(B2), 2969–2980.